PHYSICAL REVIEW B **72**, 155323 (2005)

Beyond the heteroepitaxial quantum dot: Self-assembling complex nanostructures controlled by strain and growth kinetics

J. L. Gray and R. Hull
Department of Materials Science and Engineering, University of Virginia, Charlottesville, Virginia 22904-4745, USA

Chi-Hang Lam
Department of Physics, Hong Kong Polytechnic University, Hong Kong

P. Sutter
Center for Functional Nanomaterials, Brookhaven National Laboratory, Upton, New York 11978, USA

J. Means
Department of Physics, Texas A&M University, College Station, Texas 77843, USA

J. A. Floro*
Sandia National Laboratories, Albuquerque, New Mexico 87185-1415, USA
(Received 1 June 2005; published 25 October 2005)

Heteroepitaxial growth of GeSi alloys on Si (001) under deposition conditions that partially limit surface mobility leads to an unusual form of strain-induced surface morphological evolution. We discuss a kinetic growth regime wherein pits form in a thick metastable wetting layer and, with additional deposition, evolve to a quantum dot molecule—a symmetric assembly of four quantum dots bound by the central pit. We discuss the size selection and scaling of quantum dot molecules. We then examine the key mechanism—preferred pit formation—in detail, using *ex situ* atomic force microscopy, *in situ* scanning tunneling microscopy, and kinetic Monte Carlo simulations. A picture emerges wherein localized pits appear to arise from a damped instability. When pits are annealed, they extend into an array of highly anisotropic surface grooves via a one-dimensional growth instability. Subsequent deposition on this grooved film results in a fascinating structure where compact quantum dots and molecules, as well as highly ramified quantum wires, are all simultaneously self-assembled.

DOI: 10.1103/PhysRevB.72.155323 PACS number(s): 81.07.Ta, 68.65.Hb, 61.46.+w, 81.15.Kk

INTRODUCTION

When a material is fabricated in the form of nanoscale clusters, the properties of these clusters, or quantum dots, can differ significantly from those of the corresponding bulk material. In addition to serving as a testbed for studying low-dimensional condensed matter physics, quantum confinement effects render the relevant properties size dependent, which can be very useful in the design of novel high performance devices. The overall material response in an ensemble of quantum dots not only depends on the distribution of quantum dot (QD) sizes, but on the size-dependent crystal structure and defect density, the surface structure, interactions between neighboring clusters, and interactions with any support matrix or substrate.

There are a number of fabrication schemes to produce quantum dots. Top-down approaches such as electron beam lithography can produce fine scale functional structures with fully controlled shape and placement. However, serial writing implies low throughput, and structures at or below the tens of nanometer scale are difficult to form. Solution-based self-assembly processes are very promising in that they can produce large quantities of nanoscale clusters with highly monodisperse size distributions. However, control of placement and shape is difficult, and cluster aggregation must be avoided. Heteroepitaxial self-assembly offers a means to impact near-term applications in solid-state electronics and optoelectronics. In this approach, coherent growth of a misfitting strained film on a substrate leads to growth of three-dimensional, coplanar islands (or quantum dots) that often exhibit good size selectivity. Quantum dot sizes scale inversely with the misfit strain, which can be used to manipulate the size scale. However, control over QD placement typically requires a hybrid approach using patterned surfaces to proscribe the location of QDs.

While sound technological applications underlie interest in heteroepitaxial QDs, the associated scientific issues are important and far reaching. Heteroepitaxial self-assembly yields deep insight into processes governing film growth and surface morphological evolution. Extensive effort has been expended on understanding nucleation, collective instabilities, step interactions, faceting, surface stress, elastic interactions, ripening, and phase transitions. The Ge_xSi_{1-x}/Si system is the most intensively studied heteroepitaxial materials combination. This is partly due to the obvious importance of Si and its alloys to the microelectronics industry. Further, Ge_xSi_{1-x}/Si represents a model materials system for studies of epitaxial growth and strain relaxation, with full miscibility (no intermediate phases), a reasonable range of misfit strain (the lattice parameter of Ge is 4% larger than that of Si), and a wide range of useful processing temperatures with negligible volatility of the component species.

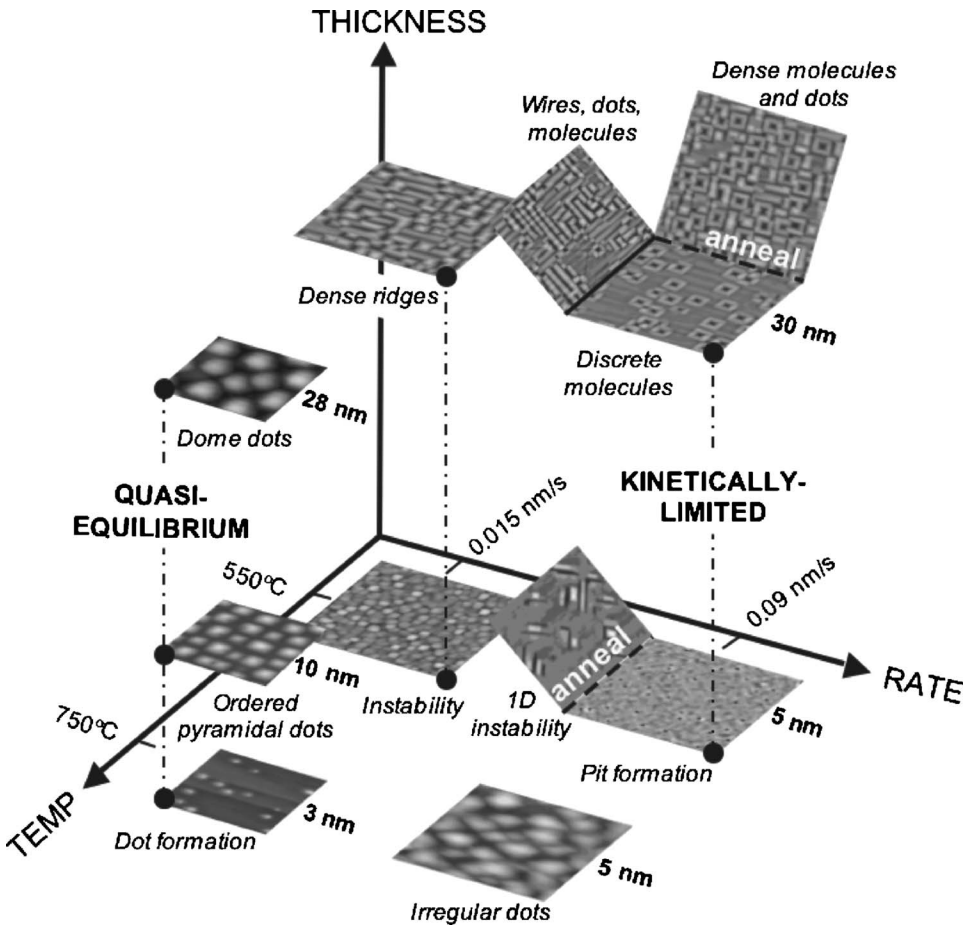

FIG. 1. The process phase-space for strain-induced morphological evolution during GeSi/Si (001) MBE growth.

Figure 1 shows a process phase space for molecular beam epitaxial (MBE) growth of strained Ge_xSi_{1-x} alloys on Si (001). The axes are deposition temperature (T_{dep}), deposition rate (R_{dep}), and mass-equivalent film thickness (h_f). The Ge fraction has been fixed at $x=0.3$ in this diagram. Much progress has been made on understanding the evolution of quantum dots in the "near-to-equilibrium" regime of high T_{dep} and low R_{dep}. Much less is understood about morphological evolution in kinetically limited growth regimes. In this paper we will show that MBE growth in the low T_{dep} and high R_{dep} regime, along with intermediate annealing steps, can be used to self-assemble potentially useful structures as indicated in Fig. 1, in the regime labeled "kinetically limited." These include not only individual quantum dots, but also fourfold quantum dot molecules (QDMs) and highly anisotropic quantum wires. Importantly, we will show that all these structures, from compact to ramified, can be self-assembled simultaneously, offering a route to self-assembled fabrication of the elements of a quantum nanocircuit. The key mechanism that underlies formation of this rich array of structures is the preferred self-assembly of pits instead of islands in the kinetically limited regime.

EXPERIMENTAL DETAILS

GeSi alloy films were grown using electron beam coevaporation in a custom-design molecular beam epitaxy (MBE) chamber. Evaporation sources were 40 cc monolithic starter sources with 99.999% initial purity. The base pressure of the chamber was below 1×10^{-10} Torr, but with a pressure of $1-2\times10^{-8}$ Torr during deposition, primarily due to hydrogen, but also with some (less than 1×10^{-9} Torr partial pressure) CO, CO_2, and CH_4. Partial pressures of O_2 and H_2O remained below 1×10^{-10} Torr. Deposition rates were controlled using calibrated quartz crystal oscillators; stoichiometry was typically within ±2 at. %, and total thickness was accurate to better than 10%. Sample heating was by radiative transfer from a nude W filament and the sample temperature was monitored using a pyrometer, with an absolute temperature accuracy of about 25 °C.

The substrates were diced from undoped Si (001) wafers, with a miscut no greater than 0.1°, to dimensions 0.5 in. $\times$1.5 in. $\times$0.012 in. thick. Cleaning for epitaxy involved chemical formation of a non-stoichiometric oxide that was ultimately removed by *in situ* desorption just before buffer growth. All chemicals were clean-room electronic grade and the rinse water was flowing, ultrafiltered 18 MΩ deionized water. After dicing, the substrates were first subjected to solvent degreasing, both in ultrasonic (2-propanol and acetone) and at elevated temperatures (trichloroethylene at 80 °C). Next, residual hydrocarbons were removed using an exothermically heated 4:1 H_2SO_4:H_2O_2 mixture. Trace transition metals were then removed using the sequence: etch in 1:1:4 HCl:H_2O_2:H_2O at 80 °C, rinse, oxide removal in 7:1 buffered oxide etch, which was repeated three times. The final

chemical oxide was formed using a 3:1:1 $HCl:H_2O_2:H_2O$ solution at 80 °C, followed by an extensive rinse, N_2 blow dry, after which the sample was immediately mounted to a Mo platen and pumped down in the MBE load lock.

After transfer into the growth chamber, samples were degassed by ramping from room temperature to 630 °C over 14–20 h. Oxide desorption occurred during 820 °C annealing for 15 min, with continuous monitoring of the surface structure using reflection high-energy electron diffraction (RHEED). A Si buffer layer was grown 100-nm thick at 750 °C, using a low/high/low sequence for the deposition rate. The RHEED pattern after buffer growth, monitored along the ⟨110⟩ azimuth, typically consisted of a Laue circle of intense spots at both integral and half-order positions, characteristic of a smooth, 2×1 reconstructed surface.

Ex situ measurements of morphology were performed using contact atomic force microscopy (AFM) using a Park Scientific Autoprobe CP. AFM images throughout this article are shown in a projected three-dimensional (3D) perspective mode, i.e., in plan view but with shadowing and reflections from an external light source that help highlight morphology. As a result, the grayscale is not a true height scale. However, in instances where relative feature heights are important, corresponding line profiles are shown. Select samples were characterized by transmission electron microscopy (TEM) using a JEOL 2000 FX.

KINETICALLY LIMITED SELF-ASSEMBLY

Growth of Ge_xSi_{1-x} alloys, with $x=0.2-0.3$, temperatures of 750 °C and deposition rates of order 0.1 monolayers/sec (ml/s), results in formation of quantum dots that follow a well-established sequence.[1,2] This is the "quasiequilibrium" regime noted in Fig. 1. For the first 1.5–2 nm, a planar wetting layer grows, but with a rapid increase in step density that eventually leads to the formation of a dense array of pyramidal islands bound by {105} facets. Formation of the dense array at low Ge fraction (low misfit strain) is thought to occur via a barrierless surface instability, followed by the onset of faceting on {105}.[3–6] Additional deposition leads to stabilization of the pyramidal shape, subsequent enlargement of the pyramids from the flux, and ripening and spatial ordering enhanced by elastic repulsion.[7,8] Eventually the pyramids reach a critical volume, whereupon they can transform into dome clusters that relieve additional strain by virtue of their higher aspect ratio, here defined as the ratio of island height to island diameter.[9–11] Finally, with further deposition, misfit dislocations enter the islands,[2] and eventually the film becomes continuous and strain relaxed. This basic sequence is observed over most of the alloy composition range, where larger Ge content leads to smaller quantum dot length scales.[2–4] At near-unity Ge fraction (4% misfit strain), similar morphological transitions still occur, but the initial formation of pyramids may now arise from a true nucleation process since the critical transition volume is small enough to be accessible via thermal fluctuations.[12]

Figure 2 shows the effect of changing the deposition conditions, for $x=0.3$. In Fig. 2(a), T_{dep} is lowered to 550 °C, but R_{dep} is kept relatively low, at about 0.1 ml/s. The

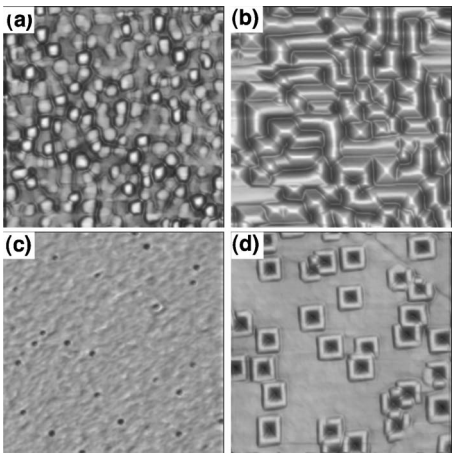

FIG. 2. $Ge_{0.3}Si_{0.7}$ films growth at 540–550 °C. (a) $R_{dep}=0.015$ nm/s, $h_f=5$ nm; (b) $R_{dep}=0.015$ nm/s, $h_f=30$ nm; (c) $R_{dep}=0.09$ nm/s, $h_f=5$ nm; (d) $R_{dep}=0.09$ nm/s, $h_f=30$ nm. AFM images are 2×2 μm.

5-nm-thick film shown in Fig. 2(a) exhibits a mounded morphology characteristic of the instability demonstrated using real-time LEEM in Refs. 3 and 4 Further deposition to a thickness of 30 nm, shown in Fig. 2(b), leads to an array of "huts"—ramified islands with {105} facets in a dense, interlaced array. Note that the troughs between ridges do not reach the Si buffer—there is a thick, metastable wetting layer below that can actually continue to increase in thickness with further deposition.[2] Thus the effect of lowering T_{dep} from 750 to 550 °C, keeping R_{dep} fixed at 0.1 ml/s is (1) to reduce roughening rates so that larger mass-equivalent film thicknesses are required for 3D roughening to proceed and (2) to retard the ability of islands to obtain the compact structure (e.g., true pyramids rather than huts) on a stable wetting layer, which would most efficiently relieve strain. These effects arise due to limitations on adatom (more precisely, addimer) mobility.

A more dramatic change occurs when the deposition rate is increased to about 0.6 ml/sec for $T_{dep}=550$ °C. Under these conditions a flat, metastable wetting layer grows to nearly 5-nm thickness, shown in Fig. 2(c). Now the initial 3D roughening occurs in the form of isolated, compact pits. With additional growth to 30 nm, Fig. 2(d), the structures enlarge, and the material ejected from the pit nucleates cooperatively[13] around the edges, forming a quantum dot molecule (QDM)—a fourfold symmetric grouping of islands bound to a central {105}-faceted pit.[14] This is the key result: under appropriate kinetically-limited growth conditions we discovered a regime in which pit formation is the preferred mechanism for strain relief,[15] and this dramatically affects morphological evolution during subsequent growth or annealing. In what follows, we try to better understand the origins of this self-assembly behavior, and to further control and manipulate the process to create potentially functional structural arrays.

Quantum dot molecules

In order to better motivate our investigation of the origins of pit formation, we first discuss the structure that results

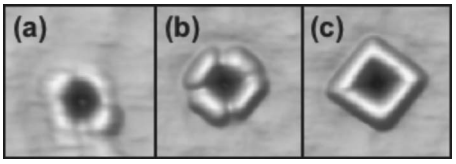

FIG. 3. Close-up images of QDMs at progressive stages of evolution. AFM images are 0.5-μm wide. The labels in each image are for reference to Fig. 4.

from preferred pit formation—the QDM. Figure 3 shows a montage of AFM images from QDMs at progressive stages of formation, while Fig. 4 shows corresponding AFM linescans and surface angle profiles, obtained as the arctan (dZ/dx) of the linescan data, where Z is the height coordinate and x is the lateral coordinate. Figure 3(a) shows an immature QDM—four discrete islands are forming about the central pit, but the linescan data shows that faceting has not

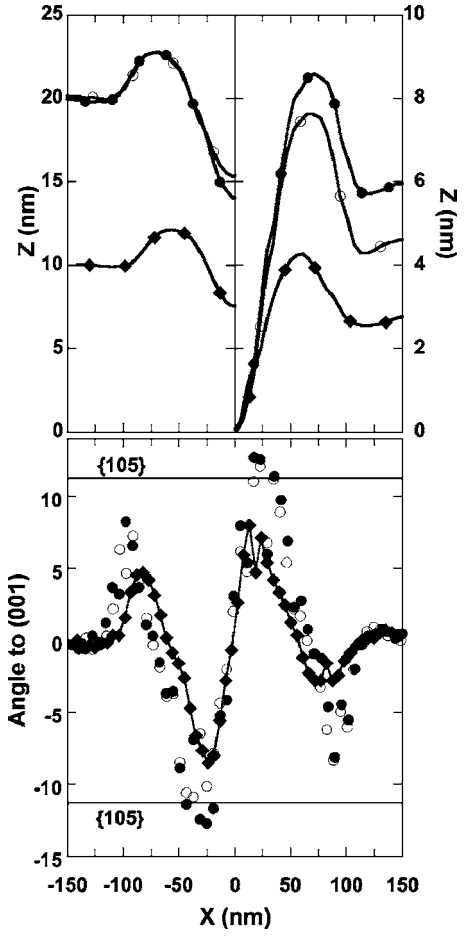

FIG. 4. (a) Line profiles through the QDMs in Fig. 3. On the left side, the profiles are drawn offset to represent the film thicknesses at which they occur, thus the bottom of the plot represents the heterointerface [note that two of the QDMs (a) and (c) in Fig. 3 occurred in the same 20-nm-thick film]. On the right side, the bottoms of the pits have been aligned, to better illustrate the shape evolution. (b) The surface angle relative to (001) from the linescan data. Diamonds from QDM (a), open circles from QDM (b), and closed circles from QDM (c).

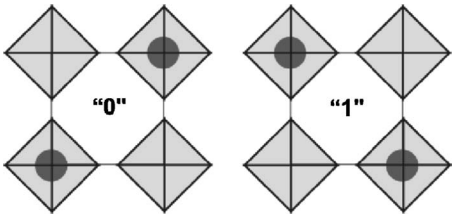

FIG. 5. The two states of a QCA cell comprised of four proximal quantum dots, two of which contain excess charge (gray circles).

yet developed (more on this in the next section). At a later stage of growth, the QDM does obtain the 11° angled {105} facets on the interior walls of the pits, although the exterior walls are not faceted. In Fig. 3(b) the islands are still discrete, while in Fig. 3(c) the islands have joined to form a continuous wall. We refer to this structure as the mature QDM.

One application to which the QDM geometry naturally lends itself is the quantum cellular automata (QCA) architecture,[16,17] whose basic concept is illustrated in Fig. 5. Extra charge in four closely spaced quantum dots will adopt one of two bistable configurations due to Coulomb repulsion, representing the two states of digital logic. Switching between states requires tunneling between adjacent dots in the cell. Logic gates can be constructed simply by an appropriate geometric alignment of cells that interact electrostatically, without the need for internal interconnects. The potential advantages of this architecture with respect to conventional Si CMOS are much lower power-delay products, and the potentially simpler interconnect schemes. One significant disadvantage is the extremely challenging lithographic requirements for practical realization of this architecture, as the dot dimensions, and even more critically the dot separations, have to be tens nanometers or less for operation at anything other than cryogenic temperatures. The configuration of the semiconductor QDM is clearly relevant to the QCA architecture, provided that a number of stringent requirements can be met, including geometric alignment of QDMs, suitable doping, carrier localization, surface passivation, narrowly distributed QDM distributions, and size scale reduction. We discuss the latter two issues next.

We showed previously that QDMs exhibit strong size selection.[18] As shown in Fig. 6, the QDM lateral (and vertical) dimensions become fixed at film thicknesses near 20 nm, and the distribution changes very little with additional deposition to over 50 nm thickness, or with annealing at T_{dep}. This implies that QDMs formed, for instance, at 20 nm, do not further enlarge as additional deposition occurs. In turn, this implies perfectly conformal growth of the QDMs once they have become stable. Empirically, size stagnation is obtained when the mature QDM structure, with its continuous bounding wall, is achieved. This apparent stability does not arise from any aspect of the energetics; we hypothesized that the formation of the bounding wall prevents escape of adatoms in the pit, thereby preventing further growth of the QDM.[18]

However, we have recently analyzed the mass conservation associated with QDMs, and the result suggests that the

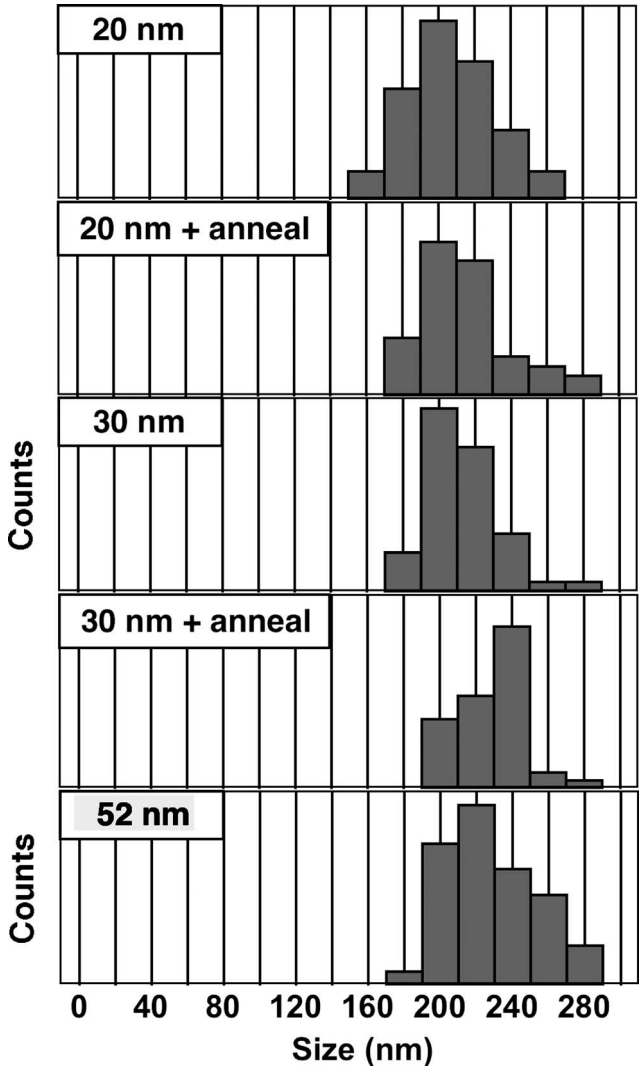

FIG. 6. Lateral size histograms for QDMs for various film thicknesses, including the effects of annealing.

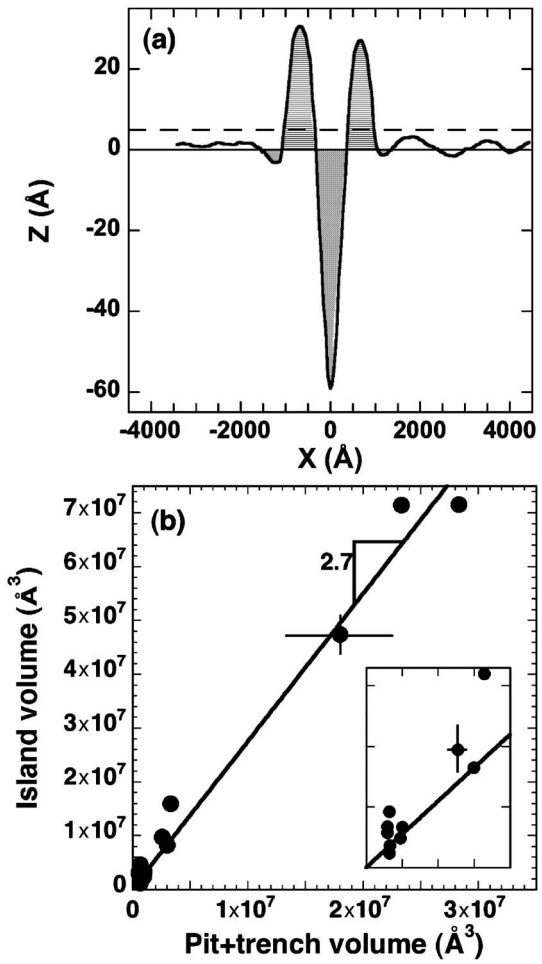

FIG. 7. (a) A linescan through a QDM defining the baseline height (solid line at $Z=0$) used for measurement of the volume of the islands (shaded above) and pit (shaded below). The dashed line shows the baseline required in order for the island volume to equal the pit+trench volume. Note that the volume measurements were done on the full 3D AFM data, not the linescan. (b) the volume in the "hill" (or islands) vs the volume in the pit (and trenches if they exist). The slope is 2.7, and typical error bars are shown for select data points. The inset magnifies the measurements in the small volume regime.

simple explanation for growth stagnation due to efficient adatom trapping within the pit is incomplete. From the AFM data we compare the volume of the islands in a QDM to the missing volume of the QDM pit. This requires determination of a baseline height associated with the "flat" regions of the film away from the QDM, as shown in Fig. 7(a), and the resulting volume measurements are quite sensitive to this baseline. Proceeding nonetheless, Fig. 7(b) shows the volume of the islands (or walls) vs the pit volume (and the volume of the shallow trenches which often surround QDMs). The data indicate that the volume in the islands is nearly 3 times larger than the pit+trench volume. This effect is larger than any error associated with baseline determination—in Fig. 7(a), the dotted baseline is that required in order to make the volume of the pit and trench equal to the island volume. This is clearly much higher than the true mean surface height.

Another source of error is tip convolution, which will exacerbate the island size relative to the pit size. However, we performed a simple convolution analysis treating the tip as a hemisphere and treating the QDM as an ideally faceted {105} structure. The result shows that for tip convolution to create an apparent $2\times$ increase in island volume to pit volume, the tip radius must equal the lateral dimension of the QDM itself, of order 250 nm. Since our tips have a nominal radius less than 20 nm, we believe that tip convolution cannot account for the mass nonconservation shown in Fig. 7(b).

Excess mass in the QDM islands implies that material is incorporated in the islands from the surrounding film (beyond that associated with the trench). While this is not surprising, it does complicate our analysis of the size selection empirically exhibited by QDMs. Even if adatoms landing in the pit cannot escape due to the continuous wall, this effect will not prevent attachment of atoms to the outer wall from the surrounding wetting layer regions, which would permit continuous enlargement of the islands at fixed pit size. Since we do not observe this, another effect must contribute to size selection. We speculate that the QDMs enlarge by mass ad-

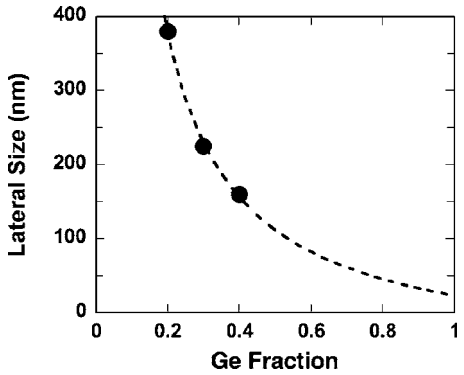

FIG. 8. The mean lateral size of QDMs vs strain (or Ge content). The dashed curve is a fit to strain^{-1}.

dition from the external wetting layer regions until the walls become large enough relative to the pit such that elastic repulsion between "islands" composing the wall prevents further growth. At this stage the island shape stabilizes and then the QDM *size* is further maintained by the kinetic effect described earlier and in Ref. 18

The QDM also exhibits an inverse scaling with the mismatch strain (or Ge content). The challenge is to find the right deposition conditions to produce preferential pit formation as a function of the strain.[19] So far we have succeeded in obtained QDMs for Ge fraction ranging from 0.25–0.40. The lateral size of the QDM as a function of Ge fraction is shown in Fig. 8, where the scaling due to strain is apparent. The data fit better to a scaling of size varying as the inverse of strain rather than the inverse square of the strain, although with only three data points and a limited range of compositions, this result is not definitive. Inverse strain scaling has been observed in quantum dot arrays by others.[3,4] These results indicate that QDMs can be formed in the true nanoscale regime, if the right deposition conditions can be identified. For pure Ge, this is likely to be an extremely small kinetic "window" requiring very large deposition rates, which may be unattainable in practice.

Pit formation

QDMs form in a kinetic regime where pits are the primary kinetic pathway for strain relaxation. The deposition conditions used in these experiments cause a metastable, thick wetting layer to form that provides a reservoir of strained material for pits to grow down into. The mechanistic origins of pits are still poorly understood, so this section provides further data and discussion that attempts to clarify this important issue. We begin by first reiterating that pits are viable strain-relieving features; in fact, pits relieve strain somewhat more efficiently than islands of equivalent size and shape.[15]

It is important to ascertain whether the pit formation observed here is an intrinsic strain relief mechanism due to the kinetic conditions, or whether the process is associated primarily with impurities or defects. Structures similar in appearance to our QDMs were observed previously when carbide contaminants present on the original Si growth surface lead to pit formation in both the *buffer* and the alloy.[20] We also observe this behavior when our MBE chamber is insufficiently clean. Under our standard vacuum conditions, however, such macropits are not observed.

Further, note that at no time during the evolution of a QDM does the central pit ever reach the GeSi/Si heterointerface. This is conclusive evidence that our QDMs do not nucleate at asperities present on the buffer surface prior to alloy growth. Cross-sectional transmission electron microscopy demonstrates that there are no threading dislocations or other obvious defects emanating from the bottom of the pit. However, we cannot completely rule out some influence by nanoscale surface defects in determining the location where pits first form. The fact that a flat buffer and an initially flat wetting layer can be grown implies that such defects would have to dynamically aggregate during alloy deposition (perhaps associated with the high R_{dep}) to eventually promote pit formation. We have found that lower areal densities of QDMs are observed under the cleanest obtainable conditions in our MBE (base pressures less than 5×10^{-11} Torr), and pit formation starts at larger thicknesses, both of which are consistent with some role for dynamic defect aggregation. At this time, no firm conclusion is possible; however, even if the initial formation event of a nanoscale pit is heterogeneous, subsequent pit enlargement, faceting, and cooperative island nucleation is almost certainly intrinsically driven by strain energy reduction.

Another important issue associated with pit formation is whether pits are faceted in the earliest stages of their growth, which would suggest that they form via nucleation. True nucleation requires a fluctuation from the locally flat (001) surface to form a fully faceted pit having a critical volume defined by the balance between elastic and surface energy.[15] A lack of faceting would indicate that instabilities somehow govern pit formation. We first examine detailed ex situ AFM images of pit evolution in the early stages of their growth.

Ex situ AFM

Figure 9 shows AFM topographs of pit evolution for film thicknesses of (a) 7.2 nm, (b) 8.4 nm, and (c) 10.2 nm. Corresponding linescans are shown in Fig. 10(a), while Fig. 10(b) shows the surface angle profile. At 7.2 nm, a low density of shallow pits formed, of order 0.5–0.7 nm deep, with maximum surface angles of 2°–2.5°. With increasing film thickness, the pits enlarge and the surrounding islands gradually become more prominent. Figure 10(a) suggests that, even as the pit enlarges, there is still adatom attachment at the bottom of the pit, which moves away from the heterointerface as deposition proceeds. At h_f=10.2 nm, the larger pits are bordered by four discrete islands, arranged along the ⟨100⟩ in-plane directions. This is the incipient QDM structure.

Even at the smallest film thickness (7.2 nm), the lateral dimension of the pit and its associated mounds is about 150 nm, which is already 68% of the final lateral dimension of the mature QDM. Thus the lateral length scale is established early in the process, clearly relating to the intrinsic length scale associated with strain-driven roughening. During these early stages of pit formation, no obvious faceting is observed—the local surface slope appears to continuously

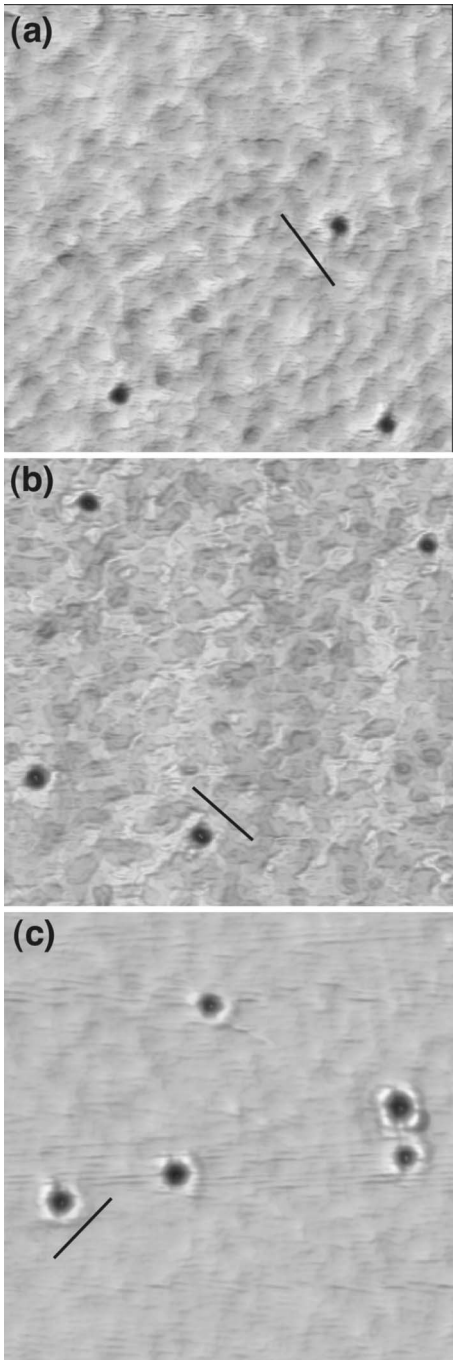

FIG. 9. Pits forming at h_f=(a) 7.2 nm, (b) 8.4 nm, and (c) 10.2 nm. The lines show the linescan directions for Fig. 10, and have been offset so that the pits can be clearly seen. AFM images are 1.3×1.3 μm.

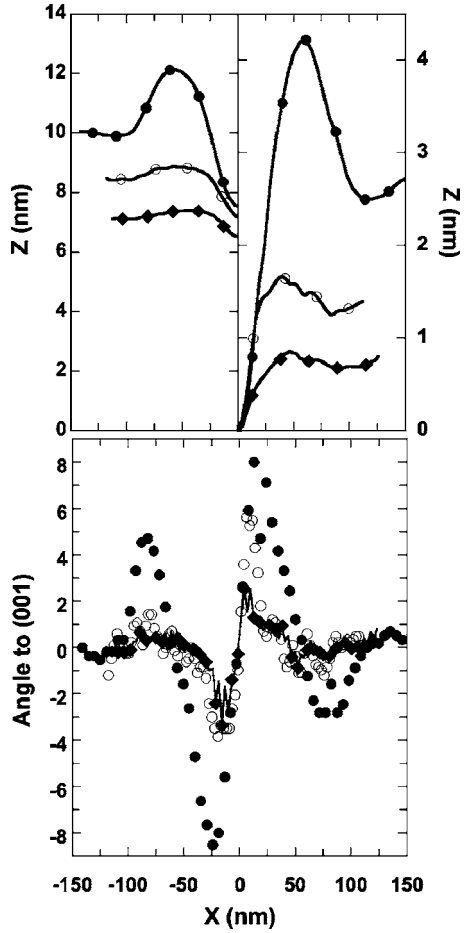

FIG. 10. (a) Line profiles through the pits in Fig. 9. On the left side, the profiles are drawn offset to represent the film thicknesses at which they occur, thus the bottom of the plot represents the heterointerface. On the right side, the bottoms of the pits have been aligned, to better illustrate the shape evolution. (b) The surface angle relative to (001) from the linescan data. Diamonds from pit (i), open circles from pit (ii), and closed circles from pit (iii).

vary as a function of lateral position. Furthermore, as a function of film thickness, the maximum local slope appears to continuously increase, at least until {105} facets form in the later stages of evolution.[21] This result suggests that pits do not form via nucleation.

In situ STM

To obtain a higher resolution view of pits, free of any surface oxide, GeSi growth was performed in a unique magnetron-sputtering-based MBE with *in situ* scanning tunneling microscopy (STM). The STM is capable of obtaining image sizes in excess of 2 μm^2 with atomic resolution (32 kilopixel)/scan line), thus combining the superior image statistics of large scan areas with full atomic detail, which is ideal given the low areal density of our pits arrays. Figure 11 shows a first image obtained on a $Ge_{0.3}Si_{0.7}$ film grown at 550 °C and 0.09 nm/s to a film thickness of 5 nm. Numerous shallow pits (islands), 2–3 ml deep (high) are observed, typical of growth under kinetically limited conditions. However, a small fraction of the pits are deeper, 5–7 ml deep, with local maximum surface angles of 3°–6°. The linescan in Fig. 11 highlights one such pit. These pits occur with a density similar to those shown in Fig. 9 and we will assume here that they are the same type of structure. The STM shows that the outer edges of the pits have an inverse wedding cake structure of $2\times n$ reconstructed (001) terraces and steps, but in the central portion of each pit there is a small, deep hole (see the linescan in Fig. 11). The hole in the linescan of Fig. 11 is only 3 monolayers deep with a measured sidewall angle of 5°–6°, but we cannot rule out tip convolution affects for

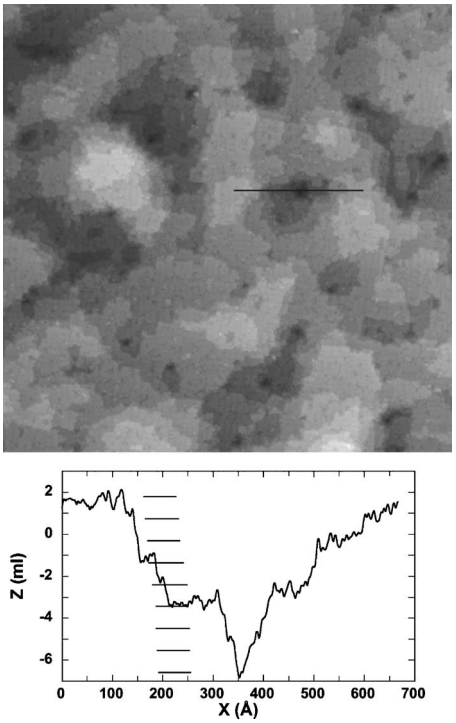

FIG. 11. 230×230 nm *in situ* STM image (part of a larger 1.1 μm scan) of a $Ge_{0.3}Si_{0.7}/Si$ (001) film grown by magnetron sputtering using the nominal QDM deposition parameters. A linescan across a deeper pit (location identified by the line on the image) is shown in the lower panel.

this small structure. At this time we are not able to resolve whether this central region is truly faceted, or simply is the cusp of a cracklike structure where steps have bunched. Additional STM images at different thicknesses and further analysis will be published elsewhere.

Kinetic Monte Carlo simulations

Recently, two-dimensional kinetic Monte Carlo (KMC) simulations of Ge/Si heteroepitaxy identified three different regimes of roughening as a function of deposition rate at fixed deposition temperature.[22] At low deposition rate, discrete islands formed from an initial instability. At very high rates, the film remained flat to the largest thicknesses simulated. However, at intermediate deposition rates, the film grew as a thick, metastable wetting layer, followed by formation of discrete pits as the preferred strain relief mechanism. Given the apparent correspondence of this behavior to our experimental results, we have extended the KMC simulations to focus on pit formation for lower strains and a wider range of deposition parameters. The film and substrate system is modeled by a square lattice of balls and springs representing atoms and elastic interactions. The substrate consists of 2048×2048 atoms. Its lattice constant $a_s = 2.72$ Å which gives an atomic density consistent with that of silicon. Periodic boundary conditions in the lateral direction are assumed. Nearest and next-nearest-neighboring atoms are directly connected by springs with force constants 13.85 eV/a_s^2 and 6.92585 eV/a_s^2, respectively. Adatom diffusion, which plays a central role in the morphological evolution, is simulated using an activated hopping algorithm. Specifically, every topmost atom m in the film can hop to another random site within a distance of ±20 columns at a rate $R_0 \exp[-(n_m\gamma - \Delta E_m - E_0)/k_BT]$. Here, $n_m\gamma$ is a bond energy term with γ and n_m denoting, respectively, the bond strength and the number of nearest- and next-nearest neighbors of atom m. We take $\gamma = 0.4$ eV. An elastic energy term ΔE_m is defined as the difference in the strain energy of the whole lattice at mechanical equilibrium when the site is occupied versus unoccupied. According to this hopping rate, poorly coordinated or highly strained atoms hop preferentially as expected intuitively. We also put $E_0 = 0.53$ eV and $R_0 = 7.24 \times 10^{10}$ s^{-1} following Ref. 22. Elastic couplings of adatoms with the rest of the system are neglected and surface steps of more than two atoms high are forbidden. Accelerated algorithms including a Green's function approach for the repeated calculation of the lattice elastic energy have been used. A simulation reported here involves up to 4×10^8 hopping events and takes 10 days to execute on a 3 GHz Pentium computer.

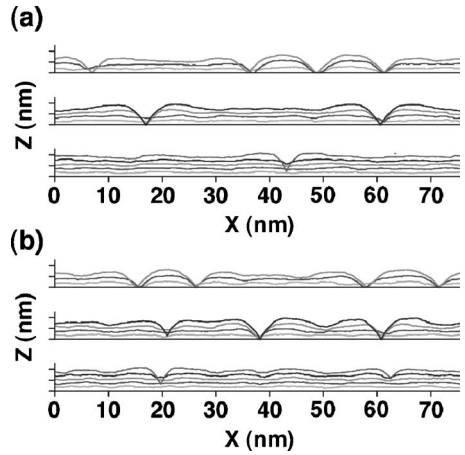

FIG. 12. Surface height profiles resulting from 2D KMC calculations for $Ge_{0.5}Si_{0.5}/Si$ (01) growth. (a) $T_{dep} = 450$ °C, with $R_{dep} = 1$ ml/s (top), 2 ml/s (middle), and 4 ml/s (bottom). (b) $T_{dep} = 550$ °C, with $R_{dep} = 10$ ml/s (top), 20 ml/s (middle), and 40 ml/s (bottom). In all panels, each contour represents a thickness increment of 20 ml, and the Z scale ticks are every 2 nm.

Figure 12 shows select KMC simulation results for Ge_xSi_{1-x} growth ($x = 0.5$) at 450 and 550 °C. The evolving surface contours are shown as a function of deposited film thickness.[23] The range of deposition rates over which pits preferentially form depends strongly on both the deposition temperature and the composition. For fixed composition, higher deposition temperatures require much higher deposition rates in order to observe pit formation. Figure 12 shows that at lower rates, pits form earlier and more frequently from the correlated instability. In this regime, pits quickly penetrate to the heterointerface. At higher rates, the rate of pit formation and enlargement is clearly retarded. Pits that form early will reach the heterointerface, but pits that form at larger thicknesses often do not penetrate completely downwards to the interface. Shallow islands are observed next to pits as material accumulates preferentially alongside the

strain-relieving pit edge. However, the effect is weaker than observed in experiment.

Detailed examination of the simulation results provides a picture that qualitatively reconciles how localized pit formation can occur via instability rather than nucleation. Under kinetically limited growth conditions, reduced adatom mobility can stabilize the wetting layer to thicknesses well above the equilibrium value, suppressing the large-scale collective instability. If the adatom mobility is too low, roughening will not occur even for very large thicknesses (in real experiments, of course, misfit dislocations will eventually enter the film as the preferred relaxation mode, but this alternative is not captured in our simulations). However, under appropriate deposition conditions, there can be just enough diffusion to permit the surface instability to operate, but the correlated surface-height "wave" is strongly damped after a few wavelengths, effectively localizing the development of roughness. The local "patches" of instability can be evanescent, smoothing out again as deposition continues. But in some cases, the trough in between two mounds can stabilize into a pit, and the material ejected from the pit accumulates alongside the pit via cooperative nucleation, forming an incipient QDM.

Several issues must be noted. (1) Two-dimensional KMC produces no true facets, and faceting is clearly important to the final QDM structure. (2) The detailed nature of the surface reconstruction and step structure is not accounted for. (3) Pits in the KMC model either grow to the heterointerface or maintain fixed distance from the interface, while our previous experiments have shown that the pit associated with a mature QDM actually moves *away* from the heterointerface.[18] (4) The KMC model has no mechanism to produce an equilibrium wetting layer. (5) Deposition parameters from KMC that lead to pit formation do not match well with experiment. In particular, we have not been able to reproduce pit formation at Ge fraction=0.3 by KMC. This may only be possible at larger lattice size and at the expense of much longer run time.

Nonetheless, the view of a damped instability forming local patches of 3D roughness that lead to discrete pit formation (and ultimately, formation of QDMs) seems plausible, and is in reasonable qualitative agreement with experiment. However, more extensive *in situ* STM analysis is needed to develop a definitive picture of the detailed pit formation mechanism.

Simultaneous formation of compact and extended structures

We have shown previously that stopping growth while in the early stage of pit formation, and then annealing the pit array at the deposition temperature (550 °C), causes a 1D instability wherein the pits elongate into grooves that can be 20× longer than they are wide.[24] A representative micrograph is shown in Fig. 13. The detailed mechanism for the lengthening instability is still not well understood. The simplest reasonable explanation is geometric in origin: the formation of islands surrounding the pit does not proceed initially with ideal four-fold symmetry. It is often the case that one or more sides of the pit are not bounded by islands—see Fig. 9. Thus, during annealing, the pit can grow laterally more easily in the direction of an unbounded side, initiating anisotropic extension of the pit. The ejected material will tend to accumulate on the already-nucleated islands on the bounded sides of the pit, thus forming the groove and ridge structure shown in Fig. 13.

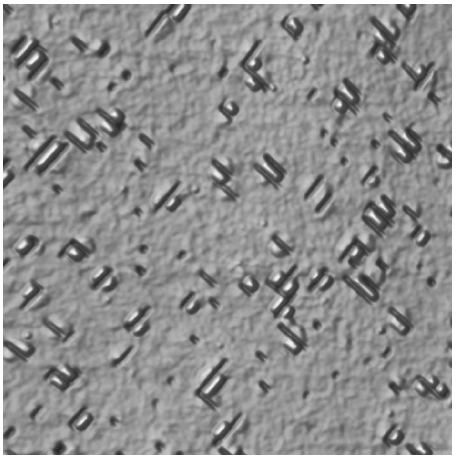

FIG. 13. Annealing a 5-nm-thick sample containing only pits [similar to Fig. 9(a)] at the deposition temperature for 1 h produces an array of faceted grooves and a variety of island shapes. The AFM image is 4×4 μm.

When additional material is deposited on the groove and ridge structure, the resulting morphology is shown in Fig. 14. While quite complex, there are several notable features. The structure contains a mix of highly anisotropic wirelike features, QDMs, and individual quantum dots. Clearly the wires and quantum dots form due to cooperative nucleation[13] due to the presence of the initial groove and ridge structure created during the anneal. Pits that did not elongate during the annealing step, or newly formed pits during deposition, serve as the sites for symmetric QDM formation. Thus, by inserting a simple annealing step into the standard QDM growth recipe, we have significantly modified the morphological evolution, enabling simultaneous self-assembly of both compact (QDMs and QDs) and extended (wires) features.

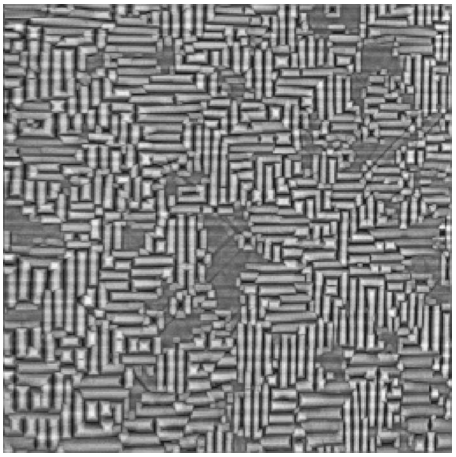

FIG. 14. The morphology resulting from the sequence: growth of $Ge_{0.3}Si_{0.7}$ at 550 °C, 0.09 nm/s, to 5 nm thickness, annealing *in situ* for 1 h at 550 °C, continued alloy growth to 30 nm total thickness at 550 °C, 0.09 nm/s. The AFM image is 5×5 μm.

If we view QDMs as logic elements in the QCA architecture, QDs as storage elements for charge, and wires as interconnects, then we have, in essence, self-assembled the primary components of a logic circuit. Of course, we are actually still very far from self-assembling functional logic. Our structures are randomly located, they are at too large a length scale, they will not yet confine charge efficiently at room temperature (since the wetting layer and the morphological features are nominally of the same composition), and they are not doped, passivated or isolated. However, some of these issues can be addressed. Features such as dots and QDMs can be located precisely using substrate prepatterning, e.g., with a focused ion beam.[25,26] Length scale reduction can be accomplished by growing with higher Ge content (see Fig. 8). Better charge confinement will require that the dots and wires have enriched Ge content compared to the underlying matrix–this may be possible using prepatterning approaches, and we are examining whether there may be a tendency for QDMs to naturally enrich with Ge compared to the wetting layer.

SUMMARY

Additional degrees of freedom in strain-induced surface morphological evolution are obtained through the manipulation of the deposition parameters during GeSi/Si MBE. Growth in a kinetic regime where surface diffusion is reduced but not entirely suppressed results in the preferred formation of pits in a metastable wetting layer. These pits appear to be intrinsic, self-assembled features associated with a damped surface instability. Additional deposition on the pits leads to the formation of quantum dot molecules—bound, fourfold symmetric configurations of a central {105} pit and four islands that could be useful in the quantum cellular automata computing architecture. QDMs exhibit good size selection, due to a combination of effects including intrinsic length scaling, a shape that exhibits a local minimum in elastic energy due to interisland elastic repulsion effects, and efficient capture of adatoms within the central pit. By inserting an annealing step within the QDM growth process, we elongate pits into highly anisotropic grooves and ridges. Subsequent growth on this morphology leads to simultaneous self-assembly of wires, dots, and molecules. This work provides both progress and some promise towards the goal of functional self-assembled nanologic circuits, although many challenges still remain.

ACKNOWLEDGMENTS

The authors acknowledge helpful discussions with J. Tersoff, L. Sander, G. Snider, F. Ross, R. Tromp, and B. Swartzentruber. Work at the UVa was performed under a Materials Research Science and Engineering Center (Grant No. DMR-0080016), and a Focused Research Group (Grant No. DMR-0075116), funded by the National Science Foundation. C.H.L. was supported by HK RGC, Grant No. PolyU-5289/02P. Work at Brookhaven was performed under the auspices of the U.S. Department of Energy under Contact No. DE-AC02-98CH10886, and was supported by NSF Grant No. DMR-0208673. Work at Sandia was supported by the DOE Office of Basic Energy Sciences. Sandia is a multiprogram laboratory of the United States Department of Energy operated by Sandia Corporation, a Lockheed Martin Company, under Contract No. DE-AC04-94AL85000.

*Email address: jafloro@sandia.gov

[1] J. A. Floro, E. Chason, R. D. Twesten, R. Q. Hwang, and L. B. Freund, Phys. Rev. Lett. **79**, 3946 (1997).
[2] J. A. Floro, E. Chason, L. B. Freund, R. D. Twesten, R. Q. Hwang, and G. A. Lucadamo, Phys. Rev. B **59**, 1990 (1999).
[3] P. Sutter and M. G. Lagally, Phys. Rev. Lett. **84**, 4637 (2000).
[4] R. M. Tromp, F. M. Ross, and M. C. Reuter, Phys. Rev. Lett. **84**, 4641 (2000).
[5] J. Tersoff, B. J. Spencer, A. Rastelli, and H. von Kanel, Phys. Rev. Lett. **89**, 196104 (2002).
[6] P. Sutter, P. Zahl, and E. Sutter, Appl. Phys. Lett. **82**, 3454 (2003).
[7] J. A. Floro, E. Chason, M. B. Sinclair, L. B. Freund, and G. A. Lucadamo, Appl. Phys. Lett. **73**, 951 (1998).
[8] J. A. Floro, M. B. Sinclair, E. Chason, L. B. Freund, R. D. Twesten, R. Q. Hwang, and G. A. Lucadamo, Phys. Rev. Lett. **84**, 701 (2000).
[9] M. Tomitori, K. Watanabe, M. Kobayashi, and O. Nishikawa, Appl. Surf. Sci. **76/77**, 322 (1994).
[10] F. M. Ross, J. Tersoff, and R. M. Tromp, Phys. Rev. Lett. **80**, 984 (1998).
[11] J. A. Floro, G. A. Lucadamo, E. Chason, L. B. Freund, M. Sinclair, R. D. Twesten, and R. Q. Hwang, Phys. Rev. Lett. **80**, 4717 (1998).
[12] D. E. Jesson, M. Kastner, and B. Voigtlander, Phys. Rev. Lett. **84**, 330 (2000).
[13] D. E. Jesson, K. M. Chen, S. J. Pennycook, T. Thundat, and R. J. Warmack, Phys. Rev. Lett. **77**, 1330 (1996).
[14] J. L. Gray, R. Hull, and J. A. Floro, Appl. Phys. Lett. **81**, 2445 (2002).
[15] J. Tersoff and F. K. LeGoues, Phys. Rev. Lett. **72**, 3570 (1994).
[16] C. S. Lent and P. D. Tougaw, Proc. IEEE **85**, 541 (1997).
[17] I. Amlani, A. O. Orlov, G. Toth, G. H. Bernstein, C. S. Lent, and G. L. Snider, Science **284**, 289 (1999).
[18] J. L. Gray, N. Singh, D. M. Elzey, R. Hull, and J. A. Floro, Phys. Rev. Lett. **92**, 135504 (2004).
[19] T. E. Vandervelde, P. Kumar, T. Kobayashi, J. L. Gray, T. Pernell, J. A. Floro, R. Hull, and J. C. Bean, Appl. Phys. Lett. **83**, 5205 (2003).
[20] M. Krishnamurthy, J. S. Drucker, and J. A. Venables, J. Appl. Phys. **69**, 6461 (1991).
[21] We note that a better approach to searching for preferred facets would be to construct surface angle histograms from the full areal data of the AFM images, such as those shown in Ref. 6. However, the low areal density of pits, combined with the inability of our AFM to obtain reliable data over very short scan lengths, has stymied our ability to garner statistically useful

data. Hence we have relied instead on representative linescans and surface angle profiles.

[22] C-H. Lam, C-K. Lee, and L. M. Sander, Phys. Rev. Lett. **89**, 216102 (2002).

[23] Surface evolution movies found at http://apricot.ap.polyu.edu.hk/pit

[24] J. L. Gray, R. Hull, and J. A. Floro, Appl. Phys. Lett. **85**, 3253 (2004).

[25] M. Kammler, R. Hull, M. C. Reuter, and F. M. Ross, Appl. Phys. Lett. **82**, 1093 (2003).

[26] J. L. Gray, S. Atha, R. Hull, and J. A. Floro, Nano Lett. **4**, 2447 (2004).